



Grain boundary engineered metal nanowire cocatalysts for enhanced photocatalytic reduction of carbon dioxide

Yuzhen Zhu^a, Zaixiang Xu^a, Qingqing Lang^a, Wenya Jiang^b, Qiaoqiao Yin^a, Shuxian Zhong^a, Song Bai^{a,b,*}

^a Key Laboratory of the Ministry of Education for Advanced Catalysis Materials, College of Chemistry and Life Sciences, Zhejiang Normal University, Jinhua, Zhejiang 321004, PR China

^b Hefei National Laboratory for Physical Sciences at the Microscale, School of Chemistry and Materials Science, University of Science and Technology of China, Hefei, Anhui 230026, PR China

ARTICLE INFO

Article history:

Received 29 October 2016

Received in revised form 4 January 2017

Accepted 13 January 2017

Available online 15 January 2017

Keywords:

Grain boundary

Cocatalyst

Nanowire

Photocatalysis

Carbon dioxide

ABSTRACT

The combination of metal cocatalysts with light-harvesting semiconductors is a promising route to improving the photocatalytic performance in CO₂ reduction reaction. However, owing to the high H₂O activation ability of metal surface, the H₂ evolution from water as a side reaction greatly decreases the activity and selectivity for CO₂ reduction. Herein, we demonstrate that the photocatalytic performance in CO₂ reduction can be promoted by grain boundaries (GBs) on metal cocatalysts. In this work, metal (Rh and Pd) nanowires with high density of GB were loaded on TiO₂ nanosheets, which acting as cocatalysts effectively reduce the H₂ evolution and greatly enhance the photocatalytic performance in CO₂ reduction as compared with the corresponding metal nanoparticle cocatalysts without GBs. Two effects are believed to contribute to this enhancement: (1) nanowire structure facilitates the interfacial electron transfer from TiO₂ to metal cocatalysts; (2) the GB terminations on the surface of metal cocatalysts are catalytically active sites for CO₂ reduction reaction. This work highlights the rational architectural design of cocatalyst for enhanced photocatalytic performance.

© 2017 Elsevier B.V. All rights reserved.

1. Introduction

Photocatalytic reduction of carbon dioxide with water to value-added chemicals such as CO (CO₂ + 2H⁺ + 2e⁻ → CO + H₂O) and CH₄ (CO₂ + 8H⁺ + 8e⁻ → CH₄ + 2H₂O) is an attractive and green route to address the depletion of fossil fuels and concomitant global warming problem [1–4]. Since the pioneering work by Inoue et al. [5], many semiconductors, such as TiO₂ [6,7], ZnGe₂O₄ [8], CeO₂ [9], and W₁₈O₄₉ [10] have been developed as photocatalysts in CO₂ reduction reaction. Among them, TiO₂ is the most widely used semiconductor due to a number of advantages including relatively high photocatalytic activity, low cost and toxicity, and good chemical and thermal stability [2,6,7]. However, the photocatalytic efficiency of bare semiconductors in CO₂ reduction reaction is greatly limited by the serious photo-generated electron-hole recombination in the bulk semiconductor as well as high activa-

tion energy of highly stable CO₂ molecules on the semiconductor surface [11,12].

Recently, noble metal, such as Pt [13], Pd [14], Ag [15], Au [16], and Cu [17] have been widely used as reduction cocatalysts to combine with the semiconductors in promoting the photocatalytic performance in CO₂ reduction reaction. On one hand, the metal cocatalysts extract the photo-induced electrons from the semiconductors in promoting the separation of electrons and holes [18]. On the other hand, the cocatalysts serve as reaction active sites in reducing the activation potential for CO₂ molecules, thus promoting the surface reaction in CO₂ reduction [19,20]. However, as reported by our groups and others, resulted from the high H₂O activation ability of metal cocatalyst surface, the photocatalytic reduction of H₂O to H₂ (2H⁺ + 2e⁻ → H₂) is a preferential or competitive reaction during the process of CO₂ reduction, which not only reduces the product yields owing to the loss of electrons in the side reaction, but also lowers the product selectivity [7,14]. Furthermore, the electron extraction ability of the metal cocatalysts remains to be improved in realizing the high yield of products for practical applications [21].

Surface and interface design of cocatalysts is a promising route to increase the photocatalytic activity and selectivity for CO₂

* Corresponding author at: Key Laboratory of the Ministry of Education for Advanced Catalysis Materials, College of Chemistry and Life Sciences, Zhejiang Normal University, Jinhua, Zhejiang 321004, PR China.

E-mail address: songbai@zjnu.edu.cn (S. Bai).

reduction [22]. Adjusting the surface parameters of cocatalysts such as the composition, facet and phase not only realizes the high adsorption and activation ability for specific reactant molecules, but also prevents the side or back reactions [14,23,24]. While the interface parameters between the semiconductor and cocatalysts, such as interfacial area and facet, can be tailored to enhance the efficiency of electron transfer from semiconductor to the cocatalyst for surface reduction reaction [25,26]. Herein, we demonstrate that the photocatalytic performance in CO₂ reduction reaction can be promoted through increasing the density of grain boundary (GB) on the metal cocatalysts. In this work, metal (Rh and Pd) nanowires with high density of GBs were *in situ* grown on TiO₂ nanosheets to form semiconductor nanosheet supported nanowire cocatalyst hybrid structures. It was found that the nanowire structure facilitated the interfacial electron transfer from TiO₂ to metal cocatalysts, while the GB terminations on the surface of metal cocatalysts acted as highly active reaction sites for CO₂ reduction. As a result, both the photocatalytic CO₂ reduction activity and selectivity of the nanowire cocatalysts were superior to those of corresponding metal nanoparticle cocatalysts without GBs. As far as we known, it is the first report on the GB engineering on the surface of cocatalyst for enhanced photocatalytic performance.

2. Experimental

2.1. Chemicals

Sodium hexachlororhodate(III) (Na₃RhCl₆, Aldrich, 206288), poly(vinyl pyrrolidone) (PVP, M.W. ≈ 55000, Aldrich, 856568), sodium iodide (NaI, Aladdin, S104084) and sodium tetrachloropalladate(II) (K₂PdCl₄, Aladdin, P106044) were used in the synthesis. All other chemicals were of analytical grade and purchased from Sinopharm Chemical Reagent Co., Ltd. All the chemicals were used as received without further purification. The water used in all experiments was de-ionized (DI).

2.2. Preparation of photocatalysts

2.2.1. Synthesis of TiO₂ nanosheets

The TiO₂ nanosheets were synthesized by modifying a method in literature with hydrofluoric acid as a capping agent [27]. Caution! Hydrofluoric acid is extremely corrosive and toxic, and should be handled with extreme care.

2.2.2. Synthesis of TiO₂-Rh samples

In a typical synthesis, Na₃RhCl₆ (10 mg), NaI (75 mg), sodium ascorbate (NaAA, 40 mg) and PVP (160 mg) were dissolved in a mixture of 5 mL ethylene glycol (EG) and 1 mL H₂O suspension containing 100 mg TiO₂ nanosheets. The mixture was sonicated for around 5 min and heated at 170 °C for 5 min and 30 min to obtain TiO₂ nanosheets supported short and long Rh nanowires, respectively [28]. The as-obtained products were collected by centrifugating and washing several times with acetone, water and ethanol, and drying at 45 °C in vacuum. TiO₂ nanosheets supported Rh nanoparticles was prepared under the same experimental conditions as the TiO₂ supported Rh nanowires except without use of NaI, which was heated at 170 °C for 30 min. The TiO₂ nanosheets supported long Rh nanowires was further annealed at 280 °C under Ar protection for 3 h to obtain the annealed TiO₂-Rh nanowires.

2.2.3. Synthesis of TiO₂-Pd samples

In a typical synthesis of TiO₂ supported Pd nanowires, K₂PdCl₄ (7.6 mg) and PVP (800 mg) were dissolved in 10 mL of aqueous suspension containing 100 mg TiO₂ nanosheets. The resulting homogeneous suspension was transferred to a 20-mL Teflon-lined stainless-steel autoclave and then heated at 200 °C for 4 h before it

was cooled to room temperature. The as-obtained products were collected by centrifugating and washing several times with acetone, water and ethanol, and drying at 45 °C in vacuum. As for the synthesis of TiO₂ supported Pd nanoparticles, PVP (120 mg) were dissolved in 8 mL EG suspension of TiO₂ nanosheets (100 mg), which was injected into a 50-ml flask, and pre-heated under magnetic stirring at 160 °C. Then 3 mL of EG solution containing K₂PdCl₄ (7.6 mg) was then added into the flask, and the reaction was allowed to proceed at 160 °C for 3 h. The product was collected and dried at 45 °C in vacuum. The TiO₂ nanosheets supported Pd nanowires was further annealed at 280 °C under Ar protection for 3 h to obtain the annealed TiO₂-Pd nanowires.

2.3. Sample characterizations

Transmission electron microscopy (TEM) and high-resolution TEM (HRTEM) images were taken on a JEOL JEM-2100F field-emission high-resolution transmission electron microscope operated at 200 kV. Powder X-ray powder diffraction (XRD) patterns were recorded by using a Philips X'Pert Pro Super X-ray diffractometer with Cu-K α radiation ($\lambda = 1.5418 \text{ \AA}$). X-ray photoelectron spectra (XPS) were collected on an ESCALab 250 X-ray photoelectron spectrometer, using nonmonochromatized Al-K α X-ray as the excitation source. UV-vis-NIR diffuse reflectance data were recorded in the spectral region of 200–800 nm with a Shimadzu SolidSpec-3700 spectrophotometer. Photoluminescence (PL) spectra were recorded on a HITACHI F-7000 Spectrofluorometer. The molar ratios of metal to TiO₂ were measured as follows: the samples were dissolved with a mixture of HCl and HNO₃ (3:1, volume ratio), which was then diluted with 1% HNO₃. The concentrations of metal were then measured with a Thermo Scientific PlasmaQuad 3 inductively-coupled plasma mass spectrometry (ICP-MS). The weight ratios of metal to TiO₂ were determined by sample weighing prior to the dissolution of metal for the ICP-MS measurements.

2.4. Photoelectrochemical measurements

3.0-mg as-synthesized products were dispersed in a mixture of 10-μL ethanol and 10-μL nafton, which were then uniformly spin dropped onto a 1 cm × 1 cm indium tin oxide (ITO)-coated glass by a spin coater (SC-1B, China). Subsequently, the ITO-coated glass was heated at 80 °C in a vacuum oven for 1 h. The photocurrents were measured on a CHI 660D electrochemical station (Shanghai Chenhua, China) in ambient conditions under irradiation of a 300-W Xe lamp (Solaredge 700, China). UV light was used as the illumination source, which was realized by using a 400-nm cutoff filter (short-wave-pass). The power density of UV light was measured to be 2.7 mW cm⁻². Standard three-electrode setup was used with the ITO coated glass as photoelectrode, a Pt foil as counter electrode, and a Ag/AgCl electrode as reference electrode. The three electrodes were inserted in a quartz cell filled with 0.5-M Na₂SO₄ electrolyte. The photoreponse of the prepared photoelectrodes (i.e., $I-t$) was operated by measuring the photocurrent densities under chopped light irradiation (light on/off cycles: 60 s) at a bias potential of 0.4 V vs. Ag/AgCl for 400 s. The electrochemical impedance spectroscopy (EIS) was carried out in the frequency range of 10⁻¹–10⁵ Hz with an AC voltage amplitude of 10 mV at a bias potential of 0.4 V vs. Ag/AgCl.

2.5. Photocatalytic CO₂ reduction measurements

CO₂ photocatalytic reduction reaction was typically conducted in a 100 mL reactor (Perfect Light Company, Beijing). To remove possible trace organic contaminants, all the samples were treated at 160 °C for 3 h in air. The heat treatment at 160 °C can not influence the morphology of the samples with the reason that the

TiO₂-Rh and TiO₂-Pd samples were synthesized at the same or a higher temperature. In a typical process, 15 mg of photocatalyst was dispersed on the flat glass plate on the bottom of the reactor. And 1 mL H₂O was added and surrounded the plate. The reactor loaded with photocatalysts was first purged with high purity CO₂ for 30 min. The pressure of CO₂ was regulated to 0.15 MPa. Then the light-irradiation experiment was performed by using a 300 W Xe lamp with UV light as the illumination source. The power density of UV light ($\lambda < 400$ nm) was measured to be 2.7 mW cm⁻². The photocatalytic reaction was typically performed for 4 h. During the irradiation, 1 mL gas and 1 μ L liquid were sampled from the glass chamber at a given time intervals (1 h). The amounts of gaseous products evolved were determined using gas chromatography (GC-2014, Shimadzu). The H₂ and CH₄ were determined using a thermal conductivity detector (TCD) and flame ionization detectors (FID), respectively. The CO was converted to CH₄ by a methanation reactor and then analyzed by the FID. The C₂H₅OH in liquid phase was determined by a FID using gas chromatography (GC-2010 Plus, Shimadzu). During the stability test, the photocatalysts were collected after each run and then reused for the CO₂ reduction reaction. The photocatalysts were heat-treated at 160 °C for 3 h after the runs before its reusing. The apparent quantum efficiency (AQE) was measured under the same reactive condition, except for the use of a 365 nm band-pass filter instead of 400-nm cutoff filter. The AQE was calculated according to the following Equation:

$$\text{AQE} = \frac{\text{number of reacted electrons}}{\text{number of incident photons}} \times 100\% \\ = \frac{\text{number of } H_2 \text{ molecules} \times 2 + \text{number of } CO \text{ molecules} \times 2 + \text{number of } CH_4 \text{ molecules} \times 8 + \text{number of } C_2H_5OH \text{ molecules} \times 12}{\text{number of incident photons}} \times 100 \quad (1)$$

3. Results and discussion

3.1. Synthesis and characterization of TiO₂-Rh samples

The work begins with the choice of single-crystalline TiO₂ nanosheets as a semiconductor model, which was synthesized through a hydrothermal procedure according to previous report [27]. As shown in the TEM images (Fig. S1a and b), the edge length of the TiO₂ nanosheets is above 200 nm and the thickness is below 5 nm. According to the size of the nanosheets, the area percentage of the top and bottom flat faces is over 95%. The large flat surface of the TiO₂ nanosheets facilitates the loading of cocatalysts in various dimensions, while the low thickness shortens the distance of electron transfer to the cocatalyst in reducing the possibility of electron-hole recombination in the bulk semiconductor. According to the XRD pattern, the as-synthesized TiO₂ nanosheets are in anatase phase (JCPDS 21-1272) (Fig. S2). As indicated by the HRTEM images, the flat surface of the TiO₂ nanosheets is exposed with (001) facet (Fig. S1c and d).

Then Rh nanocrystals were *in-situ* grown on TiO₂ nanosheets by reducing Na₃RhCl₆ with NaAA using EG as solvent. The work function of TiO₂ (≈ 4.8 eV) is smaller than that of Rh (≈ 5.0 eV), ensuring the photogenerated electron transfer from TiO₂ to Rh [29]. Based on the different experimental conditions, Rh nanocrystals in different morphologies were synthesized (Fig. S3) [28]. Rh nanowires and nanoparticles were grown on TiO₂ nanosheets with and without NaI as structure-directing agent, respectively. Furthermore, the length of the Rh nanowires could be tailored through tuning the reaction time. Longer Rh nanowires were obtained on the TiO₂ nanosheets with a longer reaction time. Accordingly, three samples including TiO₂-supported Rh nanoparticles (TiO₂-Rh NPs), TiO₂-supported short Rh nanowires (TiO₂-Rh SWs) and TiO₂-supported long Rh nanowires (TiO₂-Rh LWS) were synthesized.

From the TEM images of as-synthesized TiO₂-Rh NPs sample (Fig. 1a and b), it could be seen that Rh nanoparticles with

an average size of 2 nm are uniformly distributed on the flat surface of TiO₂ nanosheets. As shown in the HRTEM image (Fig. 1c), the lattice fringes with interplanar spacing of 0.22 nm are indexed to the (111) plane of face-centered cubic (fcc) Rh crystals. In contrast to the TiO₂-Rh NPs sample, Rh nanoparticles in TiO₂-Rh SWs and TiO₂-Rh LWS were attached to each other to form nanowires on the flat surface of TiO₂ nanosheets. As shown in the TEM images of TiO₂-Rh SWs (Fig. 1d and e), short Rh nanowires with an average length in the range of 4–10 nm and diameter of about 2 nm are loaded on the surface of TiO₂ nanosheets. The corresponding HRTEM image also indicates the lattice spacing of 0.22 nm, consistent with the (111) plane of fcc Rh (Fig. 1f). The Rh nanowires are not in monocrystalline structure, as revealed by the discontinuous lattice fringes, which is resulted from the GBs formed on the joints of the attached Rh nanoparticles. It could be also seen that a small amount of Rh nanoparticles are coexisted with the nanowires in the TiO₂-Rh SWs sample, revealing that not all the nanoparticles were attached to each other in forming the nanowires. Different from the TiO₂-Rh SWs, all the Rh nanoparticles were interconnected to form longer nanowires in the TiO₂-Rh LWS sample. As shown in TEM images (Fig. 1g and h), the flat surface of TiO₂ nanosheets are decorated with wavy Rh nanowires in higher aspect ratio (>10). In the HRTEM image of the TiO₂-Rh LWS (Fig. 1i), it could be seen that the lattice fringes with 0.22 nm spacing are also broken off by the GBs. As a long Rh nanowire can be considered as the connections of

several short nanowires, the density of GB in TiO₂-Rh LWS is higher than that in TiO₂-Rh SWs as more GBs are formed on the new connected joints. Based on the HRTEM images, the surface densities of GB in TiO₂-Rh NPs, TiO₂-Rh SWs and TiO₂-Rh LWS were determined to be 0, 0.15 and 0.42 nm⁻¹, which were calculated by dividing the sum of all the GB surface lengths by the sum of the nanowire surface area according to the schematic illustration and equation in Fig. S4.

The composition of the as-obtained TiO₂-Rh samples was further confirmed by XPS spectra. The survey XPS spectrum in Fig. 2a shows the Ti, O and Rh peaks in the TiO₂-Rh LWS hybrid structure. In the high-resolution spectrum of Ti2p (Fig. 2b), the peaks with binding energies of 459.0 eV and 464.7 eV are attributed to Ti2p_{3/2} and Ti2p_{1/2} for Ti(IV) of the surface titania, respectively. And the peaks located at 530.0 eV and 531.6 eV in the high-resolution spectrum of O1s are assigned to O—Ti of TiO₂ and O—H of adsorbed OH groups on the TiO₂ surface, respectively (Fig. 2c). As for the spectrum of Rh3d (Fig. 2d), the binding energies of 307.2 eV (Rh3d_{5/2}) and 311.9 eV (Rh3d_{3/2}) are in good agreement with the zero valence of Rh, while trace amount of Rh (III) chemical states is also detected and shown as the doublets (308.5 and 313.2 eV), respectively, which are typical features for solution-phase synthesized Rh nanocrystals [30]. In the XRD pattern of TiO₂-Rh LWS (Fig. S2), besides of the peaks of TiO₂, the additional weak peaks are assigned to fcc Rh (JCPDS 01-1214).

3.2. Charge kinetics and photocatalytic performance of TiO₂-Rh samples

To investigate the charge kinetics of the TiO₂-Rh samples, the loading amounts of Rh in the TiO₂-Rh samples were kept the same as detected by ICP-MS (Table S1). The light absorption ability of the samples was firstly investigated by UV-vis-NIR diffuse reflectance spectra. As shown in Fig. 3a, bare TiO₂, TiO₂-Rh NPs,

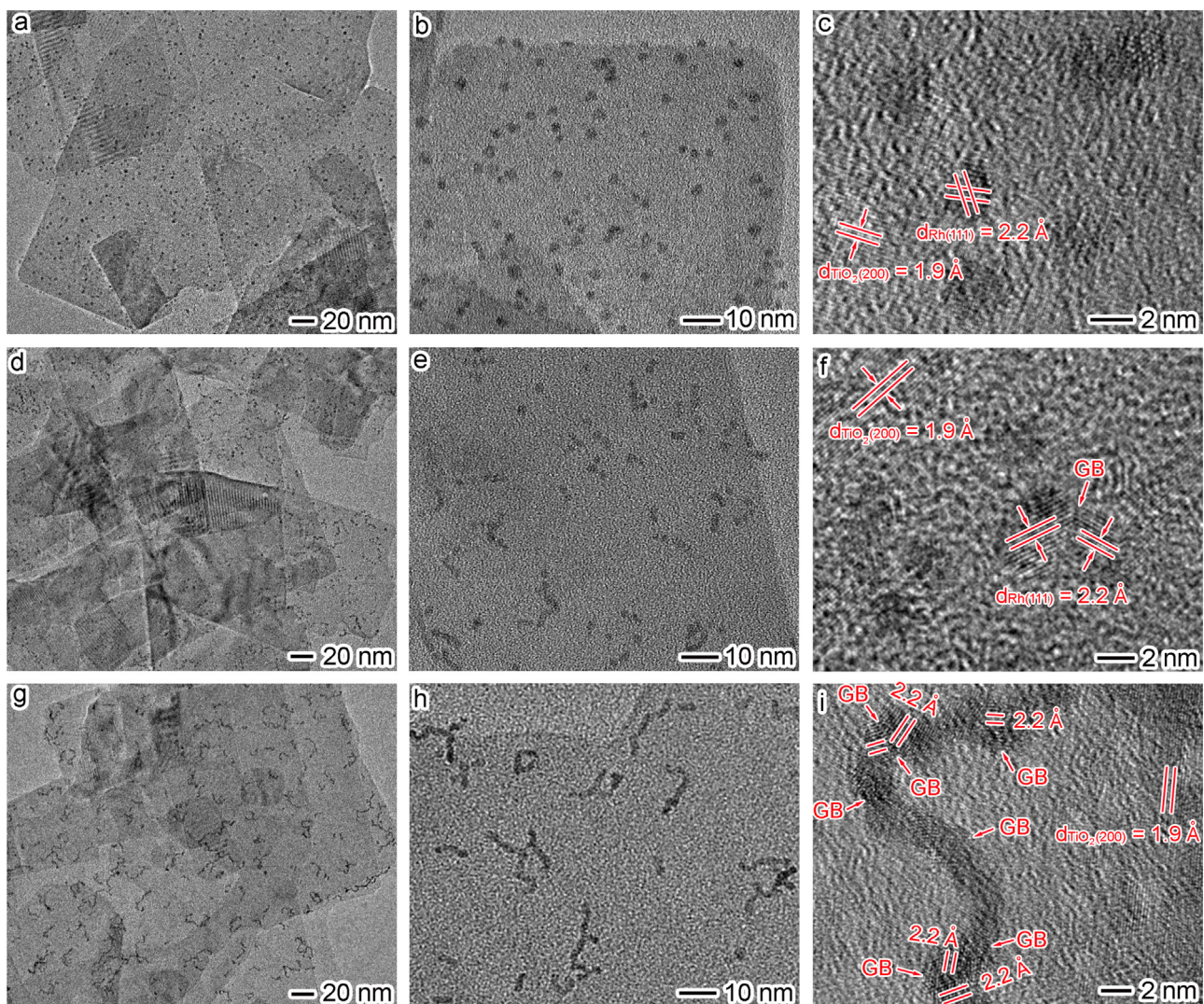


Fig. 1. TEM and HRTEM images of (a–c) TiO_2 -Rh NPs, (d–f) TiO_2 -Rh SWs and (g–i) TiO_2 -Rh LWs.

TiO_2 -Rh SWs and TiO_2 -Rh LWs exhibit comparable light absorption in UV light range ($\lambda < 400 \text{ nm}$) with absorption edge in *ca.* 390 nm, showing that the intrinsic bandgap of TiO_2 is not changed during the formation of TiO_2 -Rh hybrid structures. As both of Rh nanoparticles and nanowires barely process plasmonic absorption in the UV light region, the additional broad absorption band at $\lambda > 400 \text{ nm}$ in TiO_2 -Rh samples is resulted from the interband transition of nonplasmonic Rh [31,32]. Considering the comparable UV light absorption capability of TiO_2 -Rh samples in generating photo-induced charge carriers, the efficiency of electron-hole separation can be further reflected by photocurrent measurements. As shown in Fig. 3b, the photocurrent response under UV light irradiation is in the order of bare TiO_2 < TiO_2 -Rh NPs < TiO_2 -Rh SWs < TiO_2 -Rh LWs. This result indicates the charge extraction ability of Rh cocatalysts in promoting the electron-hole separation in TiO_2 nanosheets. Furthermore, the Rh nanowires can extract electrons from TiO_2 more effectively in comparison with Rh nanoparticles, and the charge extraction ability of which increases with the prolongation of the nanowires. The possible reason is that the anisotropic nanowire structure improves the electron transport on the Rh cocatalysts owing to the increased charge channels between the interconnected nanoparticles [33]. The higher electron transport rate on the longer nanowires efficiently prevents the accumulation of electrons on the TiO_2 -Rh interfaces, thus facilitating the interfacial electron

transfer from TiO_2 to Rh. The electron extraction ability of Rh cocatalysts is further reflected in the EIS spectra (Fig. 3c), in which the TiO_2 -Rh LWs shows a smaller arc radius as compared with TiO_2 -Rh SWs and TiO_2 -Rh NPs, suggesting that TiO_2 -Rh LWs has a lower resistance, resulted from the accelerated interfacial charge transfer between TiO_2 and Rh long nanowires. As the radiative electron-hole recombination in semiconductor induces luminescence, this argument can also be supported by PL emission spectra. As shown in Fig. 3d, in comparison with Rh nanoparticles and short Rh nanowires, the PL of TiO_2 is quenched by long Rh nanowires in larger degree, suggesting that the electron-hole recombination in TiO_2 is suppressed more efficiently by the long Rh nanowires.

Having confirmed the charge kinetics of the TiO_2 -Rh samples, we further investigated their photocatalytic performance in CO_2 reduction under UV light irradiation. The photocatalytic activity was measured in a gas-closed quartz reactor with high purity CO_2 and gaseous H_2O reactants for 4 h. The gaseous and aqueous products were continually taken from the reactor at a given interval (1 h) for quantitative analysis. H_2 , CO and CH_4 were found to be the gaseous products for CO_2 reduction, while O_2 was also detected as the product of H_2O oxidation. Besides, $\text{C}_2\text{H}_5\text{OH}$ was also detected as the liquid phase product, confirming the occurrence of this reaction: $2\text{CO}_2 + 12\text{H}^+ + 12\text{e}^- \rightarrow \text{C}_2\text{H}_5\text{OH} + 3\text{H}_2\text{O}$. Control photocatalytic experiment under the same condition but in the absence of CO_2

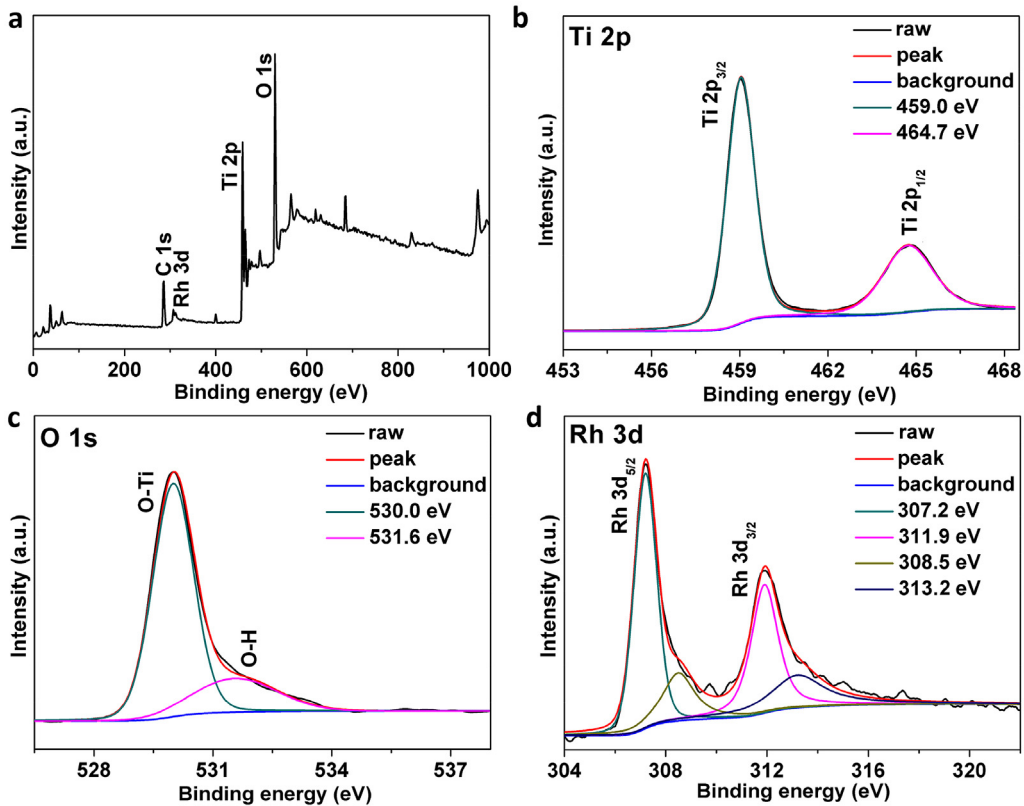


Fig. 2. XPS spectra of TiO_2 -Rh LWs: (a) survey spectrum, (b) Ti2p, (c) O1s and (d) Rh3d high-resolution spectra.

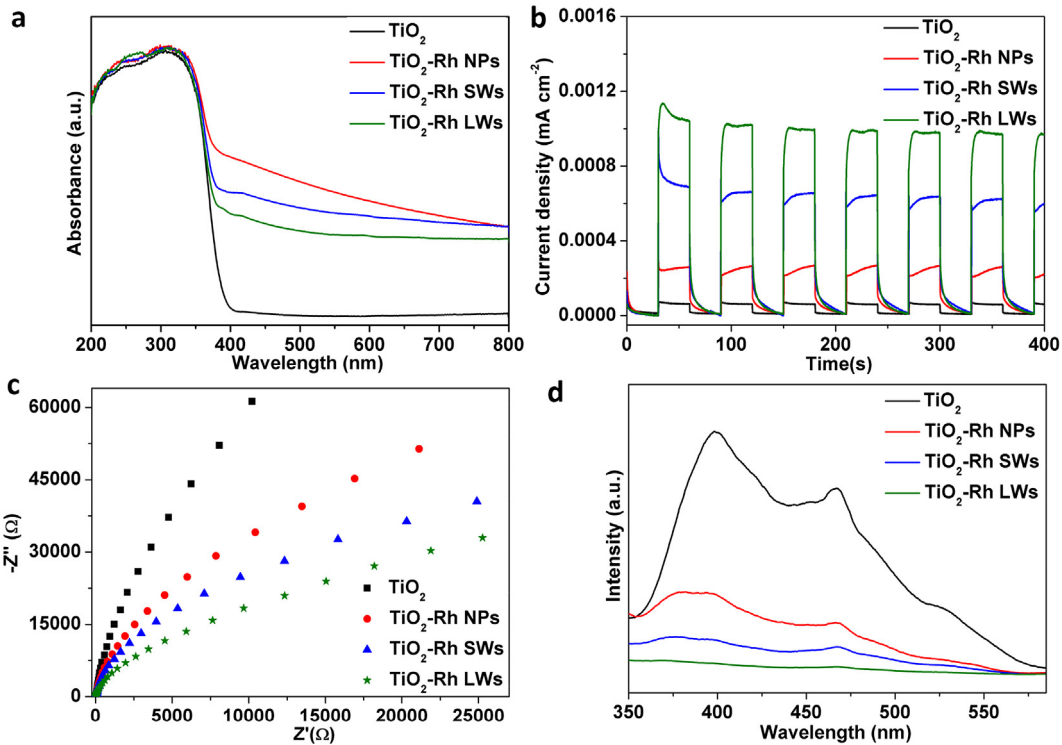


Fig. 3. (a) UV-vis-NIR diffuse reflectance spectra of TiO_2 , TiO_2 -Rh NPs, TiO_2 -Rh SWs and TiO_2 -Rh LWs; (b) photocurrent vs. time ($I-t$) curves and (c) EIS Nyquist plots of TiO_2 , TiO_2 -Rh NPs, TiO_2 -Rh SWs and TiO_2 -Rh LWs at 0.4 V vs. Ag/AgCl under UV light ($\lambda < 400$ nm) irradiation; (d) PL spectra of TiO_2 , TiO_2 -Rh NPs, TiO_2 -Rh SWs and TiO_2 -Rh LWs excited at 310 nm.

atmosphere was also performed, in which no carbonaceous product was detected. Fig. 4 shows the evolution of the produced H_2 ,

CO , CH_4 and $\text{C}_2\text{H}_5\text{OH}$ as functions of irradiation time. It could be seen that the yield of products increases upon prolonged light

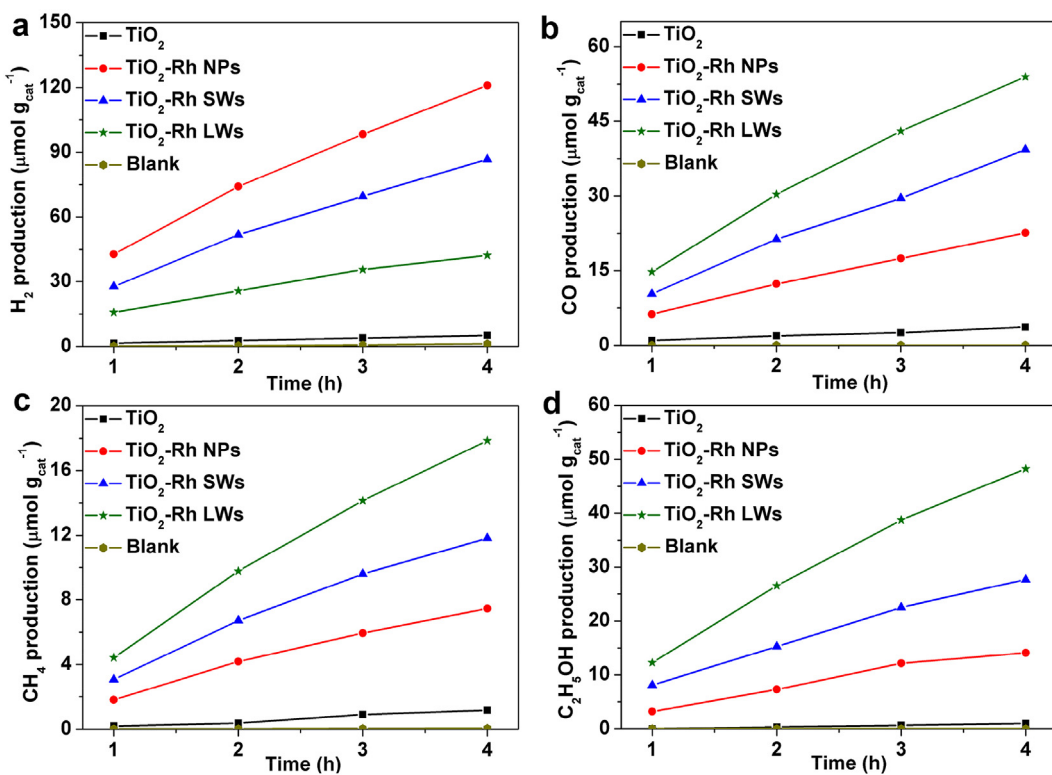


Fig. 4. Time-dependent (a) H₂, (b) CO, (c) CH₄ and (d) C₂H₅OH generated on bare TiO₂, TiO₂-Rh NPs, TiO₂-Rh SWs and TiO₂-Rh LWS in photocatalytic CO₂ reduction reaction.

irradiation for all the tested samples. In comparison with bare TiO₂, all the TiO₂-Rh samples exhibit significantly higher activity in the production of H₂, CO, CH₄ and C₂H₅OH, confirming the cocatalyst roles of Rh nanocrystals in the photocatalytic reaction. More importantly, for TiO₂-Rh samples, Rh cocatalysts with different morphologies lead to different photocatalytic activities. As shown in Fig. 4a, the H₂ yield is in the order of TiO₂-Rh NPs > TiO₂-Rh SWs > TiO₂-Rh LWS, while the CO, CH₄ and C₂H₅OH yields are in the reverse order (Fig. 4b-d). The TiO₂-Rh LWS achieves the highest CO (13.5 μmol g⁻¹ h⁻¹), CH₄ (4.5 μmol g⁻¹ h⁻¹) and C₂H₅OH (12.1 μmol g⁻¹ h⁻¹) average production rate, but the lowest H₂ average production rate (10.6 μmol g⁻¹ h⁻¹) during the 4 h reaction. As a result, the selectivity of TiO₂-Rh LWS (ca. 90.8%) for CO₂ reduction is significantly higher than those of TiO₂-Rh NPs (ca. 53.1%) and TiO₂-Rh SWs (ca. 76.0%), which is calculated through the equation according to the numbers of electrons required to produce CO, CH₄, C₂H₅OH and H₂:

$$\text{Selectivity}(\%) = \frac{[2\nu(\text{CO}) + 8\nu(\text{CH}_4) + 12\nu(\text{C}_2\text{H}_5\text{OH})]/[2\nu(\text{CO}) + 8\nu(\text{CH}_4) + 12\nu(\text{C}_2\text{H}_5\text{OH}) + 2\nu(\text{H}_2)] \times 100\%}{(2)}$$

where $\nu(\text{H}_2)$, $\nu(\text{CO})$, $\nu(\text{CH}_4)$ and $\nu(\text{C}_2\text{H}_5\text{OH})$ stand for the average formation rates for H₂, CO, CH₄ and C₂H₅OH, respectively.

The AQE of the TiO₂-Rh LWS was measured to be 0.32% at 365 nm, higher than those of the TiO₂-Rh NPs (0.18%) and TiO₂-Rh SWs (0.26%). The higher solar-to-chemical energy conversion efficiency of TiO₂-Rh LWS is in agreement with the charge kinetics result that Rh long nanowires can extract more electrons for photocatalytic reduction reactions. Furthermore, the enrichment of electron density on Rh nanowires also enhance the probability of the eight electron reaction to CH₄ as well as the twelve electron reaction to C₂H₅OH, in contrast to the two electron reactions to CO and H₂ [34]. The photocatalytic selectivity of CH₄ and C₂H₅OH formation for TiO₂-Rh NPs, TiO₂-Rh SWs and TiO₂-Rh LWS samples are 44.3%, 65.1% and 79.0%, respectively, which is calculated through

the equation:

$$\begin{aligned} \text{Selectivity}(\%) = & [8\nu(\text{CH}_4) + 12\nu(\text{C}_2\text{H}_5\text{OH})]/[2\nu(\text{CO}) \\ & + 8\nu(\text{CH}_4) + 12\nu(\text{C}_2\text{H}_5\text{OH}) + 2\nu(\text{H}_2)] \times 100\% \end{aligned} \quad (3)$$

As the H₂ yield is not increased in the TiO₂-Rh LWS as compared with TiO₂-Rh NPs and TiO₂-Rh SWs, the boosted photocatalytic selectivity for CO₂ reduction may be attributed to not only the promoted interfacial electron transfer from TiO₂ to Rh nanowires, but also the enhanced adsorption and activation ability of CO₂ molecules on the surface of Rh nanowires. Considering the same (111) planes on the surface of Rh nanoparticles and nanowires, the unique GBs on Rh nanowires may contribute to the enhancement of photocatalytic performance. As GB is a kind of two-dimensional defect with their terminations on the surface of the crystals, there are many terraces, steps, kinks, adatoms, and vacancies on the GB surface terminations, which may act as highly active reaction sites for the adsorption and activation of CO₂ molecules.

To verify this possibility, we further reduced the density of GB on the surface of long Rh nanowires through annealing treatment of the TiO₂-Rh LWS at 280 °C under Ar atmosphere, in which atomic rearrangement was realized to obtain a more thermodynamically favorable state in minimizing the total surface energy with the reason that the GB is a kind of defect in higher surface energy. As shown in the TEM and HRTEM images of the annealed TiO₂-Rh LWS (A-TiO₂-Rh LWS) (Fig. 5a,b), the number of GB terminations on the surface of long Rh nanowires significantly decreases in spite that the nanowire shape is well maintained on the TiO₂ nanosheets. The GB density of A-TiO₂-Rh LWS has decreased from 0.42 to 0.11 nm⁻¹ after the annealing treatment. In comparison with TiO₂-Rh LWS, there is an obvious enhancement in the photocurrent response of A-TiO₂-Rh LWS (Fig. 5c). The reason is that the annealing treatment further increases the interfacial contact between TiO₂ and Rh nanowires for electron transfer, which could

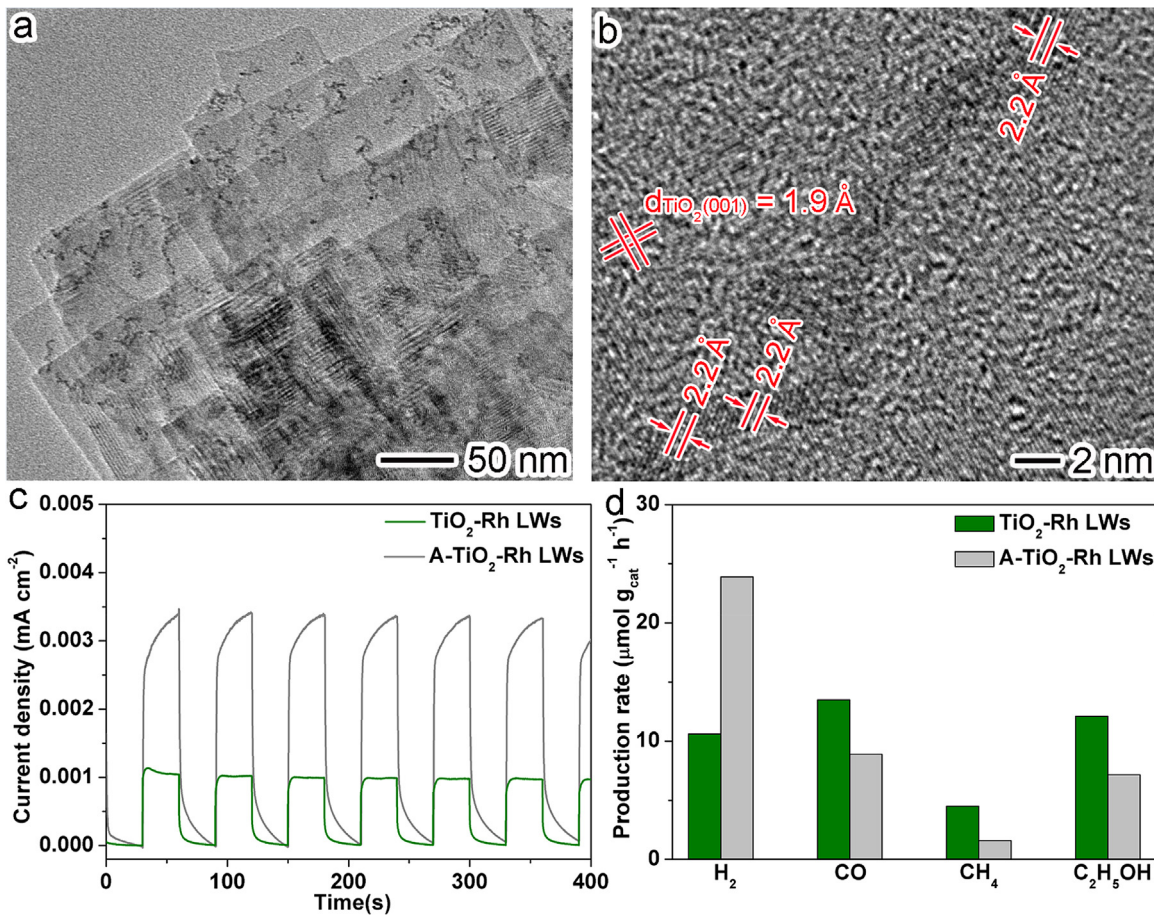


Fig. 5. (a) TEM and (b) HRTEM images of A-TiO₂-Rh LWS; (c) photocurrent vs. time (*I-t*) curves and (d) average production rate of H₂, CO, CH₄ and C₂H₅OH for A-TiO₂-Rh LWS in comparison with TiO₂-Rh LWS.

also be confirmed by the further enhanced quench degree of the PL spectra (Fig. S5). However, after the annealing treatment, the CO, CH₄ and C₂H₅OH average production rates decrease obviously, while the H₂ production rate increases for the A-TiO₂-Rh LWS sample (Fig. 5d). As a result, the selectivity for CO₂ reduction declines from 90.8% to 70.9%. The results confirm the vital function of GB terminations in promoting the photocatalytic CO₂ reduction reaction. Similarly, the recent studies have also confirmed the role of GB surface terminations as reaction active sites in the electrocatalytic reduction of CO₂ and CO [35,36]. As the similar role of electrocatalysts and cocatalysts in extracting electrons for reduction reactions on the surface [37,38], the GB terminations on the surface of Rh cocatalyst are considered to be the catalytically active sites for CO₂ reduction reaction. Based on the data of TiO₂-Rh NPs, TiO₂-Rh SWs and TiO₂-Rh LWS samples, the correlation between the GB surface density and average production rate of CO, CH₄ and C₂H₅OH was given in Fig. S6. It was found that the density of GB is not proportional to the photocatalytic activity in CO production as they should be in electrocatalysis though both the edge of electrocatalysts and cocatalysts act as electron donor and catalytically active sites for CO₂ reduction. However, the density of GB is in proportion to the CH₄ and C₂H₅OH production rate. The possible reason is that the CO is an important intermediate in the reduction of CO₂ to CH₄ (CO + 6H⁺ + 6e⁻ → CH₄ + H₂O) [4]. As a result, the actual yield of CO is not only dependent on the production rate, but also the consumption rate, which leads to the more complicated relationship between the actual CO production rate and GB surface density, rather than a proportional one.

Furthermore, the TiO₂-Rh LWS samples with higher and lower Rh loading were also synthesized, which were named as TiO₂-Rh LWS(H) and TiO₂-Rh LWS(L), respectively (Fig. S7a-c). As determined by the ICP-MS (Table S1), the loading amounts of Rh in TiO₂-Rh LWS(H) and TiO₂-Rh LWS(L) are about half and double of the original TiO₂-Rh LWS sample, respectively. The photocatalytic performance of the TiO₂-Rh LWS with different loading amounts of Rh was compared in Fig. S7d. In comparison with TiO₂-Rh LWS, it was found that both the TiO₂-Rh LWS(H) and TiO₂-Rh LWS(L) exhibit lower CO, CH₄, C₂H₅OH and H₂ production rate, confirming that there is an optimal Rh loading amount in obtaining the maximal photocatalytic CO₂ reduction activity of TiO₂-Rh LWS, which is in agreement with previous reports [13,15,39]. The possible reason is that too small amount of Rh can not effectively suppress the recombination of electron-hole pairs, while excess Rh cocatalysts not only serve as the recombination centers in decreasing the photocatalytic activity, but also mask the TiO₂ surface and reduce the light absorption. It should be noted that there is no significant difference in the photocatalytic selectivity for CO₂ reduction between the TiO₂-Rh LWS samples with different Rh loading, revealing that the photocatalytic selectivity for CO₂ reduction is not greatly dependent on the loading amount of Rh cocatalysts.

3.3. Photocatalytic mechanism verification with TiO₂-Pd samples

To further confirm the role of GB terminations on the surface of metal cocatalysts in the photocatalytic CO₂ reduction reaction, Pd nanoparticles and nanowires were also *in-situ* grown on TiO₂

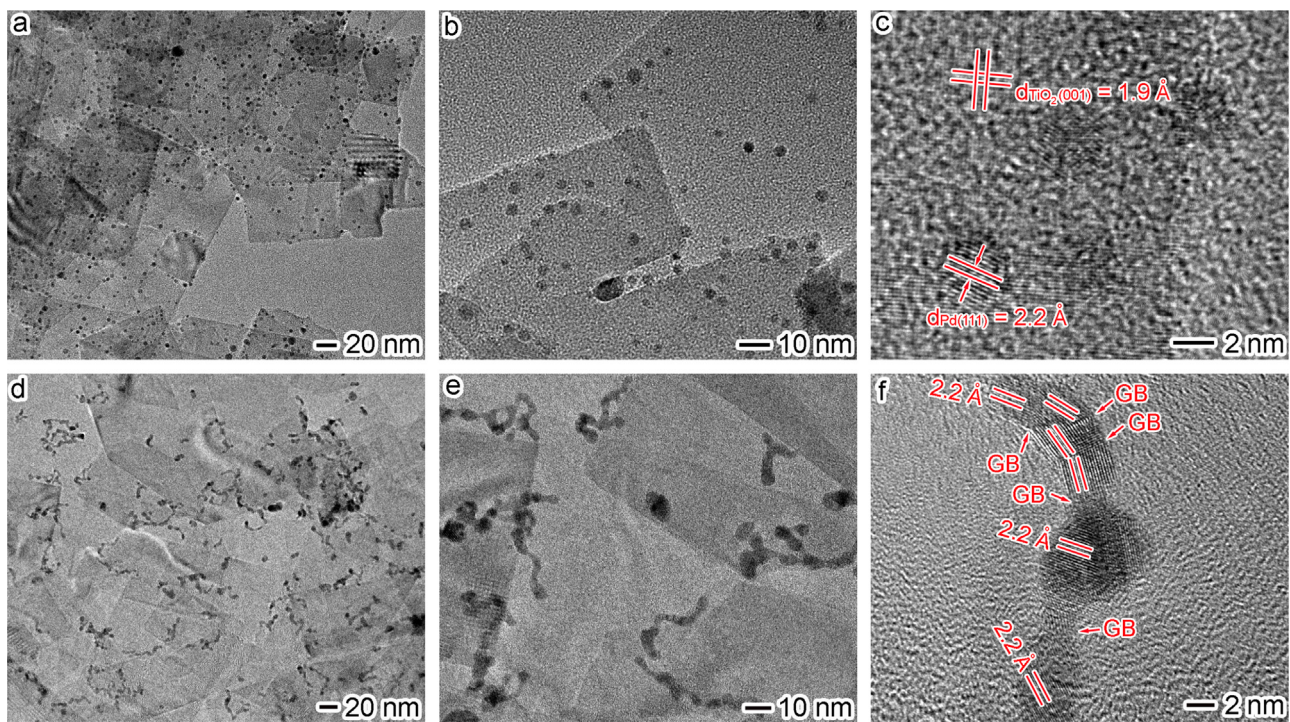


Fig. 6. TEM and HRTEM images of (a–c) TiO_2 -Pd NPs and (d–f) TiO_2 -Pd NWs.

nanosheets to form TiO_2 -Pd NPs and TiO_2 -Pd NWs samples, respectively (Fig. S8). The photo-induced electrons generated in TiO_2 can also transfer to Pd owing to the larger work function of Pd (≈ 5.1 eV) as compared with that of TiO_2 [40]. As illustrated in the TEM images of as-obtained TiO_2 -Pd NPs (Fig. 6a and b), Pd nanoparticles with an average diameter of 3 nm are uniformly deposited on the surface of TiO_2 nanosheets. In the HRTEM image (Fig. 6c), the lattice fringes with interplanar spacing of 0.22 nm are consistent with the (111) planes of fcc Pd. In the TEM images of TiO_2 -Pd NWs (Fig. 6d and e), wavy Pd nanowires with an average diameter of 4 nm and aspect ratio larger than 10 are deposited on the TiO_2 nanosheets. From the HRTEM image in Fig. 6f, it could be clearly seen that the lattice fringes with 0.22 nm interplaner spacing are also broken by GB terminations on the surface of Pd nanowires. The GB surface density is 0 and 0.32 nm^{-1} for TiO_2 -Pd NPs and TiO_2 -Pd NWs, respectively. The XPS spectra of the as-obtained TiO_2 -Pd NWs indicate the Ti, O and Pd elements in the as-obtained TiO_2 -Pd NWs sample (Fig. S9a). Among them, the Ti and O peaks are much similar to those in the XPS spectra of TiO_2 -Rh LWs (Fig. S9b,c), while Pd peaks at 335.0 eV ($\text{Pd}3\text{d}_{5/2}$) and 340.3 eV ($\text{Pd}3\text{d}_{3/2}$) are in good agreement with the zero valence of Pd, and the satellite doublets at 336.2 and 341.8 eV correspond to the trace amount of Pd(II) (Fig. S9d), which are typical features for the Pd nanocrystals synthesized in solution [41].

Similar to the TiO_2 -Rh photocatalysts, the charge kinetics of the TiO_2 -Pd samples were also studied with bare TiO_2 as a reference sample. The loading amounts of Pd in the TiO_2 -Pd samples were also kept the same and similar to the values of TiO_2 -Rh samples as detected by ICP-MS (Table S1). According to the UV-vis-NIR diffuse reflectance spectra (Fig. 7a), TiO_2 -Pd samples exhibit the comparable UV light absorption with bare TiO_2 in generating photo-induced charge carriers. In comparison with TiO_2 -Pd NPs, the larger photocurrent response of TiO_2 -Pd NWs in Fig. 7b reveals the superior electron extraction ability of Pd nanowires. The higher electron transfer ability on the interface between TiO_2 nanosheets and Pd nanowires is also confirmed by a smaller arc radius in the EIS spec-

tra as well as a larger quench degree in the PL spectra of the TiO_2 -Pd NWs sample (Fig. 7c and d). The charge kinetics study further confirms the key role of metal nanowire cocatalyst in realizing the high-efficient electron-hole separation in semiconductor.

The photocatalytic performance of the TiO_2 -Pd samples in CO_2 reduction reaction was shown in Fig. 8. It could be clearly seen that the TiO_2 -Pd NWs exhibit higher CO, CH_4 and $\text{C}_2\text{H}_5\text{OH}$ yields but lower H_2 production in comparison with TiO_2 -Pd NPs. The enhanced photocatalytic selectivity in CO_2 reduction (*ca.* 51.8% of TiO_2 -Pd NPs vs. *ca.* 84.2% of TiO_2 -Pd NWs) further confirms that the GB terminations on the surface of metal cocatalyst act as catalytically active sites in improving the photocatalytic performance in CO_2 reduction. It should be noted that in comparison with TiO_2 -Rh samples, the TiO_2 -Pd samples exhibit higher H_2 evolution rate, but relatively lower production rate for CO, confirming the surface composition of metal cocatalysts also plays an important role in the photocatalytic activity and selectivity in CO_2 reduction reaction.

The TiO_2 -Pd NWs was also annealed at 280°C under Ar protection for 3 h to obtain the annealed TiO_2 -Pd NWs (A- TiO_2 -Pd NWs). Different from the TiO_2 -Rh LWs sample, there is a significant change in the morphology of Pd nanowires after the annealing treatment. As shown in Fig. S10a and b, the Pd nanowires has changed into nanoparticles after the treatment. This difference may be resulted from the higher thermal stability of Rh in comparison with that of Pd. The similarity with TiO_2 -Pd NWs sample is that the GB surface density decreases from 0.32 to 0.07 nm^{-1} after the annealing treatment of the TiO_2 -Pd NWs (Fig. S10c). As a result, the average H_2 evolution rate increases while the CO, CH_4 and $\text{C}_2\text{H}_5\text{OH}$ rate decreases, leading to the drop of selectivity for CO_2 reduction from 84.2% to 65.1% (Fig. S10d). Similar to TiO_2 -Rh LWs, the TiO_2 -Pd NWs samples with higher and lower loading amounts of Pd were also synthesized (Fig. S11a–c). Different from the TiO_2 -Rh LWs, the TiO_2 -Pd NWs(H) with higher Pd loading shows higher photocatalytic activity than TiO_2 -Pd NWs and TiO_2 -Pd NWs(L) (Fig. S11d), revealing that the optimum loading amount of cocatalyst varies with different cocatalysts. But the similarity is the approximate

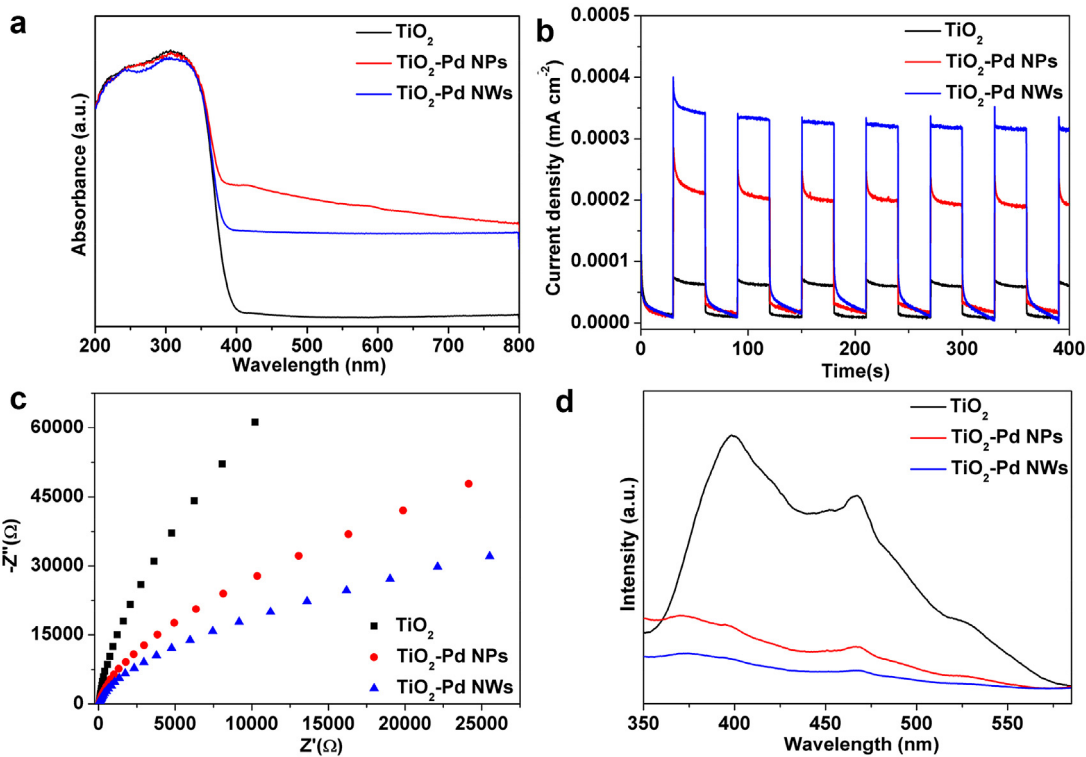


Fig. 7. (a) UV-vis-NIR diffuse reflectance spectra of TiO_2 , $\text{TiO}_2\text{-Pd NPs}$ and $\text{TiO}_2\text{-Pd NWs}$; (b) photocurrent vs. time ($I-t$) curves and (c) EIS Nyquist plots of TiO_2 , $\text{TiO}_2\text{-Pd NPs}$ and $\text{TiO}_2\text{-Pd NWs}$ at 0.4 V vs. Ag/AgCl under UV light ($\lambda < 400 \text{ nm}$) irradiation; (d) PL spectra of TiO_2 , $\text{TiO}_2\text{-Pd NPs}$ and $\text{TiO}_2\text{-Pd NWs}$ excited at 310 nm.

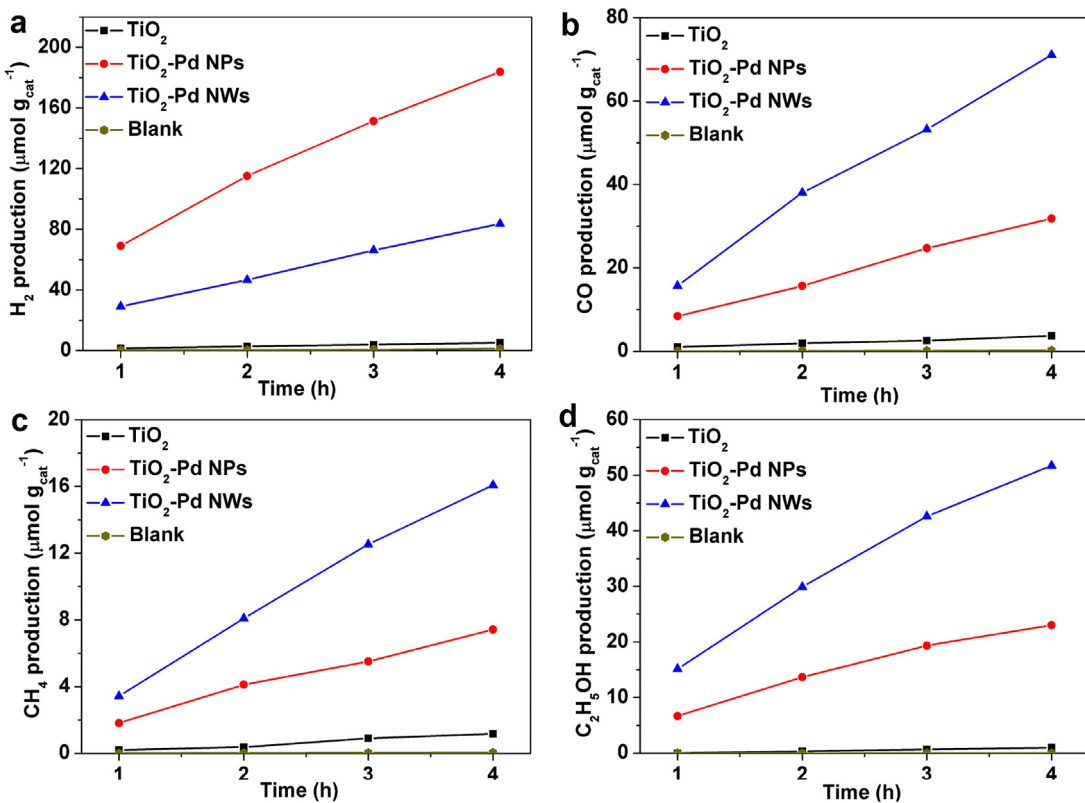


Fig. 8. Time-dependent (a) H_2 , (b) CO, (c) CH_4 and (d) $\text{C}_2\text{H}_5\text{OH}$ generated on bare TiO_2 , $\text{TiO}_2\text{-Pd NPs}$ and $\text{TiO}_2\text{-Pd NWs}$ in photocatalytic CO_2 reduction reaction.

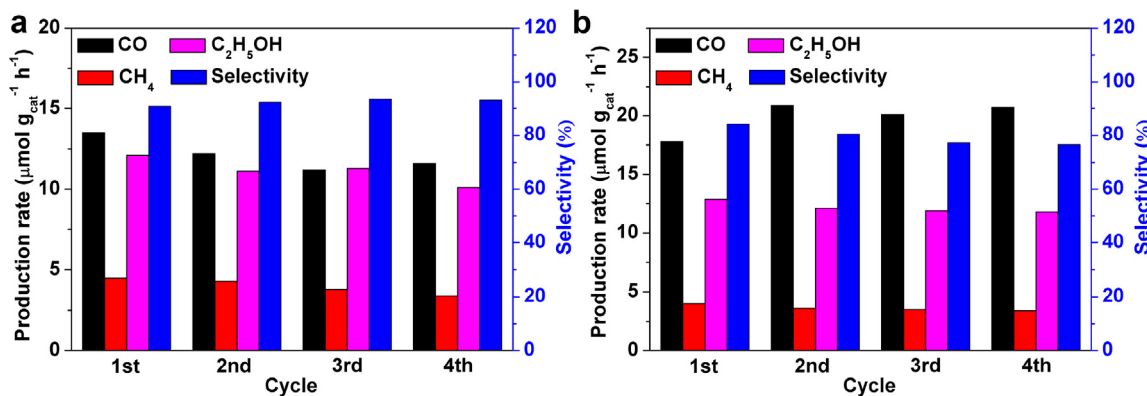


Fig. 9. Stability studies of CO, CH₄ and C₂H₅OH evolution rates as well as the selectivity for CO₂ reduction over (a) TiO₂-Rh LWs and (b) TiO₂-Pd NWs in photocatalytic CO₂ reduction reaction.

selectivity for CO₂ reduction between the TiO₂-Pd NWs samples with different Pd loading, further confirming the selectivity for CO₂ reduction is mainly dependent on the GB surface density.

3.4. Photocatalytic stability of TiO₂-Rh LWs and TiO₂-Pd NWs

As another important parameter of photocatalysts, the photocatalytic stability of the as-synthesized TiO₂-Rh LWs and TiO₂-Pd NWs in the CO₂ reduction reaction was also investigated. The photocatalysts were recollected after each run and reused for three times. As shown in Fig. 9a and b, both the TiO₂-Rh LWs and TiO₂-Pd NWs maintain good photocatalytic stability during the successive cycles. As compared with those of fresh sample, the CO, CH₄ and C₂H₅OH average production rates in the fourth run reduces by 14.1%, 24.4% and 16.5% for TiO₂-Rh LWs, respectively. Moreover, during the cycle process, resulted from more significant decrease in H₂ evolution rate, the selectivity for CO₂ reduction increases by 2.6% in the fourth run in comparison with the initial value. As for TiO₂-Pd NWs, the CO evolution rate increases by 16.3%, while CH₄ and C₂H₅OH evolution rate decreases by 15.0% and 8.5% after four cycles, respectively. In contrast to TiO₂-Rh LWs sample, a significant increase in the H₂ production rate is taken place on the TiO₂-Pd NWs along the cyclic process. As a result, the CO₂ reduction selectivity of TiO₂-Pd NWs maintains 90.5% in the fourth run. The different change trends between TiO₂-Rh LWs and TiO₂-Pd NWs in the evolution rate of products and selectivity for CO₂ reduction in the cycles further confirm the important function of surface composition in the photocatalytic reaction. The high catalytic stability may be attributed to the outstanding structural stability of the samples. As shown in Fig. S12a and c, after the photocatalytic cycles, there is no obvious change in the TEM images of TiO₂ supported metal nanowire structures compared with the fresh one. Nevertheless, it was calculated that the GB density decreased by 9.9% and 6.3% for TiO₂-Rh LWs and TiO₂-Pd NWs samples respectively, based on the HRTEM images after the stability measurement (such as Fig. S12b and d), which gives a good explanation to the slight change in the catalytic activity after a few recycles.

4. Conclusions

In summary, GB engineering was performed on the metal nanowire cocatalyst for enhanced photocatalytic performance in CO₂ reduction reaction. Rh and Pd nanowires with high density of GB were *in situ* grown on TiO₂ nanosheets to form semiconductor nanosheet supported metal nanowire cocatalyst hybrid structures. In comparison with the corresponding metal nanoparticles, the nanowire structure of metal realizes the charge flow between the interconnected nanoparticles and promotes the electron transfer

from TiO₂ to cocatalysts. On the other hand, the GB terminations on the surface of metal nanowire cocatalysts act as highly active reaction sites for the CO₂ reduction reaction. As a result, in comparison with TiO₂ supported metal nanoparticles, the designed structure of GB enriched metal nanowires loaded by TiO₂ not only exhibits higher photocatalytic activity in the reduction of CO₂ to CO, CH₄ and C₂H₅OH, but also effectively reduces the formation of H₂ and increases the selectivity for CO₂ reduction. This work represents an important advancement towards GB engineering on cocatalysts for enhanced photocatalytic performance.

Acknowledgements

This work was financially supported by National Natural Science Foundation of China (No. 21603191), Zhejiang Provincial Natural Science Foundation of China (No. LQ16B010001), Public Welfare Technology Application Research Plan Project of Zhejiang Province (Analysis Test Item, No. 2017C37024), and National Training Program of Innovation and Entrepreneurship for Undergraduates (No. 201610345014).

Appendix A. Supplementary data

Supplementary data associated with this article can be found, in the online version, at <http://dx.doi.org/10.1016/j.apcatb.2017.01.035>.

References

- [1] J.L. White, M.F. Baruch, J.E. Pander III, Y. Hu, I.C. Fortmeyer, J.E. Park, T. Zhang, K. Liao, J. Gu, Y. Yan, T.W. Shaw, E. Abelev, A.B. Bocarsly, Chem. Rev. 115 (2015) 12888–12935.
- [2] S.N. Habersreutner, L. Schmidt-Mende, J.K. Stolarczyk, Angew. Chem. Int. Ed. 52 (2013) 7372–7408.
- [3] W. Tu, Y. Zhou, Z. Zou, Adv. Mater. 26 (2014) 4607–4626.
- [4] S.C. Roy, O.K. Varghese, M. Paulose, C.A. Grimes, ACS Nano 4 (2010) 1259–1278.
- [5] T. Inoue, A. Fujishima, S. Konishi, K. Honda, Nature 277 (1979) 637–638.
- [6] J. Yu, J. Low, W. Xiao, P. Zhou, M. Jaroniec, J. Am. Chem. Soc. 136 (2014) 8839–8842.
- [7] Q. Zhai, S. Xie, W. Fan, Q. Zhang, Y. Wang, W. Deng, Y. Wang, Angew. Chem. Int. Ed. 52 (2013) 5776–5779.
- [8] Q. Liu, Y. Zhou, J. Kou, X. Chen, Z. Tian, J. Gao, S. Yan, Z. Zou, J. Am. Chem. Soc. 132 (2010) 14385–14387.
- [9] P. Li, Y. Zhou, Z. Zhao, Q. Xu, X. Wang, M. Xiao, Z. Zou, J. Am. Chem. Soc. 137 (2015) 9547–9550.
- [10] G. Xi, S. Ouyang, P. Li, J. Ye, Q. Ma, N. Su, H. Bai, C. Wang, Angew. Chem. Int. Ed. 51 (2012) 2395–2399.
- [11] M. Marszewski, S. Cao, J. Yu, M. Jaroniec, Mater. Horiz. 2 (2015) 261–278.
- [12] S. Bai, J. Jiang, Q. Zhang, Y. Xiong, Chem. Soc. Rev. 44 (2015) 2893–2939.
- [13] W.N. Wang, W.J. An, B. Ramalingam, S. Mukherjee, D.M. Niedzwiedzki, S. Gangopadhyay, P. Biswas, J. Am. Chem. Soc. 134 (2012) 11276–11281.

- [14] S. Bai, X. Wang, C. Hu, M. Xie, J. Jiang, Y. Xiong, *Chem. Commun.* 50 (2014) 6094–6097.
- [15] K. Iizuka, T. Wato, Y. Miseki, K. Saito, A. Kudo, *J. Am. Chem. Soc.* 133 (2011) 20863–20868.
- [16] Š. Neaču, J.A. Macia-Agullo, P. Concepcion, H. Garcia, *J. Am. Chem. Soc.* 136 (2014) 15969–15976.
- [17] O.K. Varghese, M. Paulose, T.J. LaTempa, C.A. Grimes, *Nano Lett.* 9 (2009) 731–737.
- [18] J. Yang, D. Wang, H. Han, C. Li, *Acc. Chem. Res.* 46 (2013) 1900–1909.
- [19] P. Wang, B. Huang, X. Qin, X. Zhang, Y. Dai, J. Wei, M.H. Whangbo, *Angew. Chem. Int. Ed.* 47 (2008) 7931–7933.
- [20] X. Zhu, P. Wang, B. Huang, X. Ma, X. Qin, X. Zhang, Y. Dai, *Appl. Catal. B: Environ.* 199 (2016) 315–322.
- [21] P. Wang, B. Huang, Y. Dai, M.H. Whangbo, *Phys. Chem. Chem. Phys.* 14 (2012) 9813–9825.
- [22] S. Bai, W. Yin, L. Wang, Z. Li, Y. Xiong, *RSC Adv.* 6 (2016) 57446–57463.
- [23] S. Bai, M. Xie, Q. Kong, W. Jiang, R. Qiao, Z. Li, J. Jiang, Y. Xiong, *Part. Part. Syst. Charact.* 33 (2016) 506–511.
- [24] S. Bai, L. Wang, X. Chen, J. Du, Y. Xiong, *Nano Res.* 8 (2015) 175–183.
- [25] Y. Zhu, Z. Xu, W. Jiang, W. Yin, S. Zhong, P. Gong, R. Qiao, Z. Li, S. Bai, *RSC Adv.* 6 (2016) 56800–56806.
- [26] S. Bai, X. Li, Q. Kong, R. Long, C. Wang, J. Jiang, Y. Xiong, *Adv. Mater.* 27 (2015) 3444–3452.
- [27] X. Han, Q. Kuang, M. Jin, Z. Xie, L. Zheng, *J. Am. Chem. Soc.* 131 (2009) 3152–3153.
- [28] X. Huang, Z. Zhao, Y. Chen, C.Y. Chiu, L. Ruan, Y. Liu, M. Li, X. Duan, Y. Huang, *Nano Lett.* 14 (2014) 3887–3894.
- [29] W. Jiang, S. Bai, L. Wang, X. Wang, L. Yang, Y. Li, D. Liu, X. Wang, Z. Li, J. Jiang, Y. Xiong, *Small* 12 (2016) 1640–1648.
- [30] Y.V. Larichev, O.V. Netskina, O.V. Komova, V.I. Simagina, *Int. J. Hydrogen Energy* 35 (2010) 6501–6507.
- [31] S. Sarina, H.Y. Zhu, Q. Xiao, E. Jaatinen, J. Jia, Y. Huang, Z. Zheng, H. Wu, *Angew. Chem. Int. Ed.* 53 (2014) 2935–2940.
- [32] H. Sakamoto, T. Ohara, N. Yasumoto, Y. Shiraishi, S. Ichikawa, S. Tanaka, T. Hirai, *J. Am. Chem. Soc.* 137 (2015) 9324–9332.
- [33] B.Y. Xia, H.B. Wu, Y. Yan, X.W. Lou, X. Wang, *J. Am. Chem. Soc.* 135 (2013) 9480–9485.
- [34] S. Xie, Y. Wang, Q. Zhang, W. Deng, Y. Wang, *ACS Catal.* 4 (2014) 3644–3653.
- [35] X. Feng, K. Jiang, S. Fan, M.W. Kanan, *J. Am. Chem. Soc.* 137 (2015) 4606–4609.
- [36] X. Feng, K. Jiang, S. Fan, M.W. Kanan, *ACS Cent. Sci.* 2 (2016) 169–174.
- [37] W. Bi, L. Zhang, Z. Sun, X. Li, T. Jin, X. Wu, Q. Zhang, Y. Luo, C. Wu, Y. Xie, *ACS Catal.* 6 (2016) 4253–4257.
- [38] B. Pan, S. Luo, W. Su, X. Wang, *Appl. Catal. B: Environ.* 168–169 (2015) 458–464.
- [39] K. Li, X. An, K.H. Park, M. Khraisheh, J. Tang, *Catal. Today* 224 (2014) 3–12.
- [40] S. Bai, L. Yang, C. Wang, Y. Lin, J. Lu, J. Jiang, Y. Xiong, *Angew. Chem. Int. Ed.* 54 (2015) 14810–14814.
- [41] S. Ghosh, R.K. Sahu, C.R. Raj, *Nanotechnology* 23 (2012) 385602.